

# The interplay of disk wind and dynamical ejecta in the aftermath of neutron star - black hole mergers

Rodrigo Fernández<sup>1,2</sup>, Eliot Quataert<sup>2</sup>, Josiah Schwab<sup>1,2</sup>, Daniel Kasen<sup>1,3</sup>,  
Stephan Rosswog<sup>4</sup>

<sup>1</sup> *Department of Physics, University of California, Berkeley, CA 94720, USA.*

<sup>2</sup> *Department of Astronomy & Theoretical Astrophysics Center, University of California, Berkeley, CA 94720, USA.*

<sup>3</sup> *Nuclear Science Division, Lawrence Berkeley National Laboratory, Berkeley, CA 94720, USA.*

<sup>4</sup> *The Oskar Klein Centre, Department of Astronomy, AlbaNova, Stockholm University, SE-106 91 Stockholm, Sweden.*

Submitted to MNRAS

## ABSTRACT

We explore the evolution of the different ejecta components generated during the merger of a neutron star (NS) and a black hole (BH). Our focus is the interplay between material ejected dynamically during the merger, and the wind launched on a viscous timescale by the remnant accretion disk. These components are expected to contribute to an electromagnetic transient and to produce  $r$ -process elements, each with a different signature when considered separately. Here we introduce a two-step approach to investigate their combined evolution, using two- and three-dimensional hydrodynamic simulations. Starting from the output of a merger simulation, we identify each component in the initial condition based on its phase space distribution, and evolve the accretion disk in axisymmetry. The wind blown from this disk is injected into a three-dimensional computational domain where the dynamical ejecta is evolved. We find that the wind can suppress fallback accretion on timescales longer than  $\sim 100$  ms. Due to self-similar viscous evolution, the disk accretion at late times nevertheless approaches a power-law time dependence  $\propto t^{-2.2}$ . This can power some late-time GRB engine activity, although the available energy is significantly less than in traditional fallback models. Inclusion of radioactive heating due to the  $r$ -process does not significantly affect the fallback accretion rate or the disk wind. We do not find any significant modification to the wind properties at large radius due to interaction with the dynamical ejecta. This is a consequence of the different expansion velocities of the two components.

**Key words:** accretion, accretion disks — dense matter — gravitational waves — hydrodynamics — neutrinos — nuclear reactions, nucleosynthesis, abundances

## 1 INTRODUCTION

Double neutron star (NS) or NS - black hole (BH) mergers are among the main candidates for direct detection of gravitational waves by ground based interferometers such as Advanced LIGO, Virgo, and KAGRA (e.g., Abadie et al. 2010). The ejecta from these mergers is also a prime candidate for the generation of  $r$ -process elements (e.g., Lattimer & Schramm 1974; Freiburghaus et al. 1999; Goriely et al. 2013). Radioactive decay of these elements is expected to power an electromagnetic counterpart that can aid in the localization of the gravitational wave source (Li & Paczyński 1998; Metzger et al. 2010b). Finally, these mergers are the leading candidate progenitor for short-

duration gamma-ray bursts (SGRBs; see, e.g., Berger 2014 for a recent review).

The ejection of material by tidal forces during the merger depends on a number of factors, including the mass ratio of the binary, the spin of each component, and the properties of the nuclear equation of state (e.g., Bauswein et al. 2013; Kyutoku et al. 2013). In BH-NS mergers, the amount of ejecta also depends crucially on BH spin (e.g., Foucart 2012). The gravitationally-bound part of this *dynamical ejecta* leads to fallback accretion onto the BH. Because fallback extends over timescales much longer than the viscous time of the disk, it has been proposed as a source of extended prompt emission and/or X-ray flares in the afterglows of some short gamma-ray bursts (Faber et al. 2006; Gehrels et al. 2006; Rosswog 2007). However, the gravita-

tional binding energy of material accreting on timescales longer than  $\sim 1$  s is comparable to or less than the energy injected by radioactive heating during  $r$ -process nucleosynthesis. Thus fallback accretion can potentially be suppressed when this heating is taken into account (Metzger et al. 2010a).

Furthermore, the dynamical ejecta does not exist in isolation. The accretion disk formed during the merger is an additional source of material in two ways. First, on  $\sim 100$  ms timescales, material can be unbound by neutrino energy deposition in a broad polar outflow (the *neutrino-driven wind*, McLaughlin & Surman 2005; Surman et al. 2006, 2008; Dessart et al. 2009; Wanajo & Janka 2012; Metzger & Fernández 2014; Perego et al. 2014). Second, over longer,  $\sim 1$  s timescales, energy deposition by angular momentum transport and nuclear recombination together with decreased neutrino cooling lead to substantial mass ejection in a quasi-spherical outflow (a *freezout wind*, Metzger et al. 2009; Lee et al. 2009; Fernández & Metzger 2013a; Metzger & Fernández 2014; Just et al. 2014; Fernández et al. 2015). The amount of material ejected by these two disk channels can be comparable to that in the dynamical ejecta, although its composition is expected to be less neutron rich, with observable consequences for the ensuing kilonova transient (Kasen et al. 2013; Barnes & Kasen 2013; Tanaka & Hotokezaka 2013; Tanaka et al. 2014, see also Kasen, Fernández & Metzger 2014).

While the dynamical ejecta is generally launched earlier and is faster than disk outflows, the interaction between these two components can be non-trivial. First, disk winds can modify fallback accretion relative to what is expected from purely ballistic trajectories. Conversely, part or all of the disk wind can mix with slower-moving components of the dynamical ejecta, potentially leading to different nucleosynthetic and electromagnetic signatures than predicted from the wind alone.

In this paper we examine the interplay between these components by means of two- and three-dimensional hydrodynamic simulations. Given that evolving the complete system over the timescales of interest with all the relevant physics is computationally expensive, we develop a two-stage modeling approach that takes advantage of the spatial and temporal decoupling of key processes. Starting from the output of a BH+NS merger simulation, we evolve the remnant accretion disk in axisymmetry (2D), with and without the dynamical ejecta, and including neutrino and viscous processes. This leads to the production of an axisymmetric disk wind. This wind is then sampled at a radius that approximately separates the accretion disk from the non-axisymmetric dynamical ejecta. The sampled wind is then injected into a larger, three-dimensional (3D) computational domain with an inner boundary that coincides with the wind sampling radius, and in which the dynamical ejecta is evolved. Our goal is to identify the key processes that govern the interaction between these two ejecta components using approximate modeling of the physics. Future studies will refine this analysis.

The paper is organized as follows. Section 2 describes the numerical approach employed, including the separation of the system into different ejecta components. Section 3 presents our results, including the properties of the disk wind

in 2D, the properties of fallback accretion without wind, and the interplay between these two components. Our results are summarized in Section 4, where broader observational implications are also discussed.

## 2 COMPUTATIONAL METHODOLOGY

It is infeasible to evolve the combined accretion disk plus dynamical ejecta system with all the relevant physics in 3D for the timescales of interest ( $\sim 10$  s). In particular, explicit viscous angular momentum transport requires resolving the corresponding diffusion time scale on the smallest grid cells in the simulation.

Fortunately, the (non-axisymmetric) dynamical ejecta is mostly spatially decoupled from the (largely axisymmetric) accretion disk once the initial transient phase ends, a few dynamical times after the merger. Angular momentum transport and neutrino processes operate on timescales slower than the expansion time outside radii  $\sim 10^8$  cm (§2.3), so they can be neglected in these regions to first approximation.

We thus adopt a two-stage approach to model the interaction of wind and dynamical ejecta. First, we evolve the system in axisymmetry including viscous and neutrino source terms, and measure the properties of the resulting disk wind at a radius that separates the two components. We then evolve the dynamical ejecta in 3D, using a computational domain that has its inner radial boundary at the radius where the wind properties were determined. From this inner boundary, the wind is injected into the domain. The only source terms employed in this second step are gravity and radioactive heating, leading to significant savings in computational time.

In what follows, we describe the numerical method used to evolve the hydrodynamic equations (§2.1), the initial conditions, including how we identify and separate distinct components of the merger remnant (§2.2), the sampling and injection of the wind in 3D models (§2.3), and the list of models simulated (§2.4).

### 2.1 Time-dependent hydrodynamics

The equations of hydrodynamics are solved numerically with the dimensionally-split PPM solver in FLASH3.2 (Fryxell et al. 2000; Dubey et al. 2009). The public version of the code has been modified to include a non-uniformly spaced grid (Fernández 2012), and physical source terms needed to model the evolution of merger remnant accretion disks (Fernández & Metzger 2013b,a; Metzger & Fernández 2014; Fernández et al. 2015). The equation of state is that of Timmes & Swesty (2000), with abundances of neutrons, protons, and alpha particles in nuclear statistical equilibrium. The nuclear binding energy contribution from alpha particles is included.

The two-dimensional (2D) version of the code solves the equations of mass-, poloidal momentum-, angular momentum-, energy-, and lepton number conservation in spherical polar coordinates  $(r, \theta)$ . Source terms include angular momentum transport by an anomalous shear stress using the kinematic viscosity of Shakura & Sunyaev (1973), and neutrino source terms via a leakage scheme

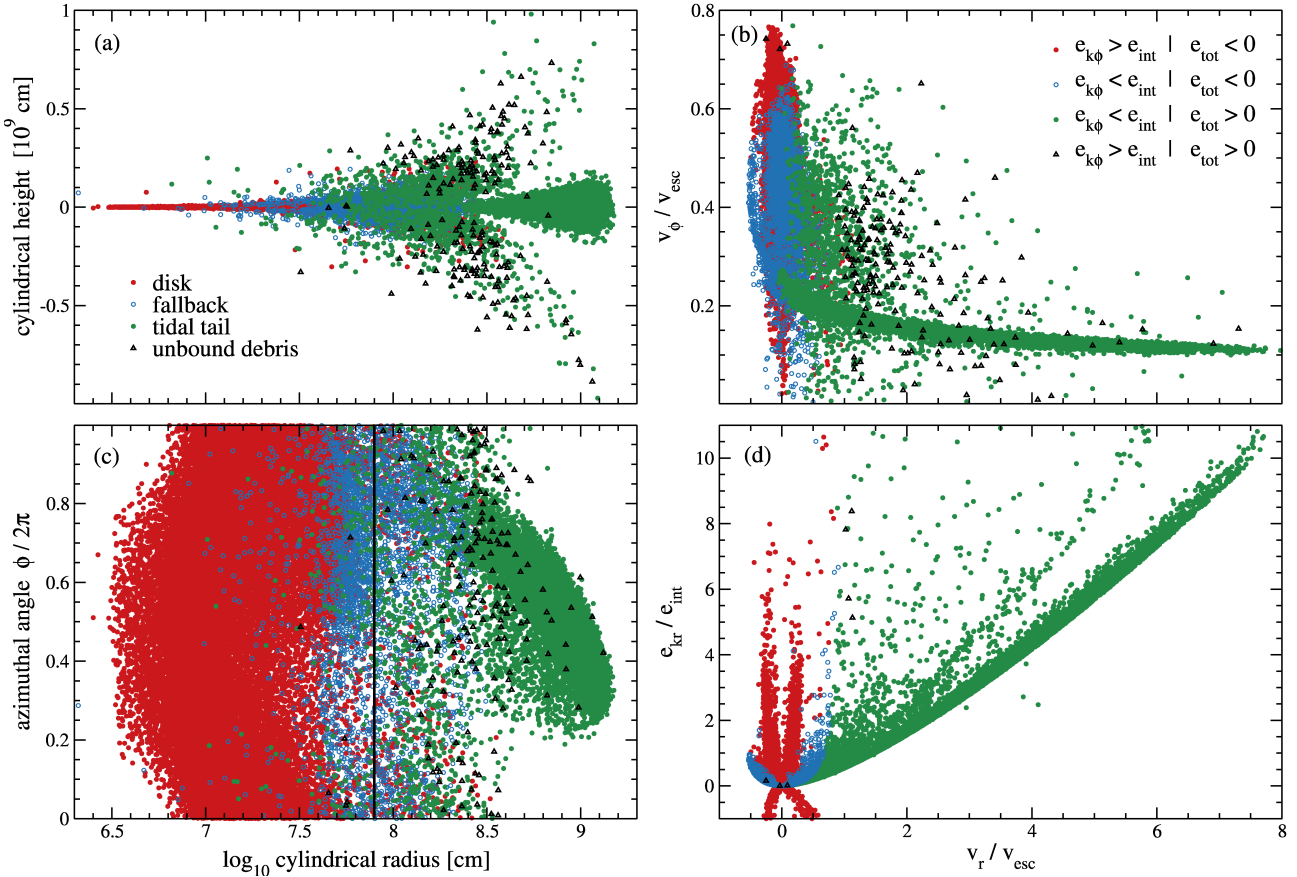


**Figure 1.** Phase space distribution of particles that comprise the initial state of the system. The disk (red solid circles), fallback (blue open circles), tidal tail (green filled circles), and unbound debris (black triangles) components are separated according to the sign of their total specific energy  $e_{\text{tot}}$ , and the ratio of the kinetic energy in the  $\phi$  direction  $e_{k\phi}$  to the internal energy  $e_{\text{int}}$ , as indicated in panel (b). The vertical line in panel (c) indicates the radius  $r_{\text{cut}}$  at which the disk wind properties are measured from 2D simulations. This radius marks the inner radial boundary of 3D models.

that only includes charge-current weak interactions (Metzger & Fernández 2014).

The three-dimensional (3D) implementation solves the equations of hydrodynamics in spherical polar coordinates  $(r, \theta, \phi)$  with gravity and radioactive heating as the only source terms. The split PPM version of FLASH3.2 requires minor modifications to be extended to 3D spherical coordinates. A description of these modifications and tests of the implementation will be presented elsewhere (Fernández 2015, in preparation). We employ the analytic parameterization of  $r$ -process radioactive heating from Korobkin et al. (2012). This source term is included in order to qualitatively assess the effect of radioactive heating on the dynamics; details such as its sensitivity to the electron fraction and spatial location are ignored. This source term is applied in cells that have temperature  $T < 5 \times 10^9$  K.

In all models, we approximate the gravitational potential of a spinning BH via the pseudo-Newtonian potential of Artemova et al. (1996). The main advantage of this potential is that it reproduces the location of the innermost stable circular orbit (ISCO) of the Kerr metric, and leads to steady-state, thin, sub-Eddington accretion disk solutions to within  $\sim 10 - 20\%$  of the exact relativistic value as computed by Artemova et al. (1996). The implied spacetime is spherically symmetric, however, so while convenient for computational

purposes, it is not a very accurate approximation for all space if the spin parameter is high. Nevertheless, since most of the material that resides at radii close to the BH – where GR effects are the strongest – lies mostly on the midplane, we consider this choice of potential as an acceptable approximation for the inner disk dynamics. At the radii where the phenomena we are interested in occur ( $r \gtrsim 10^8$  cm), GR effects are very weak (few percent or less).

The computational domain is discretized logarithmically in radius, uniformly in  $\cos\theta$  along the polar direction, and uniformly in azimuth. The resolution is 64 cells per decade in radius, 56 cells meridionally from  $\theta = 0$  to  $\theta = \pi$ , and 192 cells for  $\phi \in [0, 2\pi]$ . At the equator, cells are such that  $\Delta r/r \simeq \Delta\theta \simeq \Delta\phi \simeq 2^\circ$ . The  $(r, \theta)$  resolution is the same for most 2D and 3D models, the exception being a 2D model run at double resolution to check for convergence.

In 2D models that include the inner disk evolution, the domain covers the full range of polar angles, and extends from a radius halfway between the BH horizon and the innermost stable circular orbit (ISCO), until a radius 1000 times larger. The radial limits of 3D models are the wind injection radius  $r_{\text{cut}}$  (§2.2) on the inside, and a radius  $10^4$  times larger on the outside.

The boundary conditions are reflecting in  $\theta$  and periodic in  $\phi$ . In 2D models and 3D models with no wind injection,

both radial boundaries allow mass to leave the domain (see, e.g., Fernández & Metzger 2013a for details). When a wind is injected into a 3D model, the default boundary condition involves solution of a Riemann problem. This procedure is discussed in §2.3.

## 2.2 Initial Condition and Separation of Components

The initial condition is obtained from the output of a Newtonian Smoothed Particle Hydrodynamic (SPH) simulation of the merger of a  $10M_{\odot}$  BH with a  $1.4M_{\odot}$  NS reported in Rosswog et al. (2013). This BH mass is close to (but somewhat higher than) the peak of the inferred stellar mass BH distribution in the galaxy (e.g. Özel et al. 2010; Farr et al. 2011). The simulations use the Shen et al. (1998) equation of state, a multi-flavor, energy-integrated neutrino leakage scheme (Rosswog & Liebendörfer 2003), and Newtonian gravity with an absorbing boundary condition at the Schwarzschild radius of the (non-spinning) BH. The time of the snapshot corresponds to 139 ms after the merger.

The SPH data is mapped into the Eulerian grid using the appropriate smoothing kernel to reconstruct conserved quantities from the particle distribution. In the case of 2D simulations, data is axisymmetrized by computing azimuthal averages of conserved quantities (e.g., the radial velocity is given by  $\langle v_r \rangle = \int (\rho v_r) dV / \int \rho dV$ , with  $dV$  the volume of the cells included in the average). We use the density, temperature, and electron fraction to reconstruct the rest of the thermodynamic variables using our equation of state. If the temperature is below  $5 \times 10^9$  K, we assume full recombination into alpha particles (e.g. if  $Y_e < 0.5$ , the alpha mass fraction is set to  $2Y_e$  and the proton fraction to zero).

In order to separate the dynamical ejecta from the disk, we inspect the properties of the SPH particles in phase space and identify distinctive features. Figures 1b and 1d show the kinematic distribution of particles relative to the gravitational and internal energies. Two distinct components are evident, one that extends to large values of the radial velocity  $v_r$  relative to the escape speed  $v_{\text{esc}}$  (and hence moves ballistically), and another that clusters isotropically around zero radial velocity. The nature of these components becomes clear when they are sub-divided according to their degree of gravitational binding, quantified by the sign of the total specific energy,

$$e_{\text{tot}} = e_{\text{kr}} + e_{\text{k}\theta} + e_{\text{k}\phi} + e_{\text{int}} + e_{\text{grv}}, \quad (1)$$

and by the degree of rotational support, quantified by the ratio of rotational-kinetic to internal energies  $e_{\text{k}\phi}/e_{\text{int}}$ , where  $e_{\text{k}i}$  is the kinetic energy along the  $i$ -th direction,  $e_{\text{int}}$  is the internal energy, and  $e_{\text{grv}}$  is the gravitational energy.

We identify four components in the system:

(i) *Disk*: gravitationally bound ( $e_{\text{tot}} < 0$ ) and rotationally supported ( $e_{\text{k}\phi} > e_{\text{int}}$ ). This is the innermost component in radius and nearly axisymmetric, as shown in Figures 1a and 1c, containing most of the mass ( $0.2M_{\odot}$ ).

(ii) *Tidal tail*: gravitationally unbound and with  $e_{\text{k}\phi} < e_{\text{int}}$ . The energy is dominated by the radial kinetic energy, as shown in Figure 1, comprising a highly localized structure in phase space, outermost in radius. The mass in

this component is  $0.06M_{\odot}$ .

(iii) *Fallback*: gravitationally bound, and primarily gas pressure supported ( $e_{\text{k}\phi} < e_{\text{int}}$ ). With this definition, it includes the outermost part of the disk and the innermost part of the tidal tail, as shown most explicitly in Figure 1b. The mass in this component is  $0.02M_{\odot}$ .

(iv) *Unbound debris*: the remaining material is gravitationally unbound with significant rotation. It can be considered part of the dynamical ejecta, but it does not comprise as localized a structure as the tidal tail. The mass is  $\sim 10^{-3}M_{\odot}$ .

We follow the separate evolution of these components in our FLASH simulations using passive scalars, constructed by taking the ratio of the partial mass density formed with each sub-group of SPH particles to the total mass density. By definition, these scalars add up to unity.

Once mapped into FLASH, these components are not completely decoupled, however. Figures 1a and 1c show that there is spatial overlap between the particles, particularly around  $r \sim 10^8$  cm. This overlap leads to mixing when reconstructing the fluid distribution using the SPH kernel. Approximately  $0.01M_{\odot}$  of material initially tagged as *tidal tail* is gravitationally bound, while a very small amount of *disk* and *fallback* material ( $\simeq 10^{-3}M_{\odot}$  in total) is unbound.

We choose a radius  $r_{\text{cut}} = 800$  km to quantify the unbound properties of the disk wind in 2D axisymmetric simulations of the inner disk. This position corresponds approximately to the innermost edge of the tidal tail (Figure 1c), separating a nearly axisymmetric matter distribution on the inside from a highly non-axisymmetric one on the outside. At the time of our initial conditions (139 ms after the merger), this surface encloses 99% of the *disk* mass and 43% of the *fallback* mass.

The mass of the BH at the beginning of the simulation is approximately  $11.1M_{\odot}$ , and it is kept fixed thereafter. The inner boundary for 2D models is set at  $3.7 \times 10^6$  cm, midway between the ISCO and the event horizon of a BH with spin parameter  $a = 0.8$ . A significantly smaller spin would be inconsistent with the tidal disruption of the NS (e.g. Foucart 2012). Also, the potential of Artemova et al. (1996) asymptotes to Newtonian for very high spins, so this choice is more consistent with the physics used to generate the initial condition (a BH modeled as a Newtonian point mass with an absorbing boundary condition at the Schwarzschild radius of a non-spinning BH; Rosswog et al. 2013).

## 2.3 Wind Injection in 3D Simulations

In 2D simulations, we record the properties of the material crossing at  $r = r_{\text{cut}}$ , as a function of polar angle and at regular time intervals. Subsequent injection of this data into 3D models is achieved by interpolating the recorded variables in time for a given polar angle, copying the resulting values for all azimuthal angles.

The inner radial ghost cells of 3D models are filled by solving a Riemann problem at the inner radial boundary, taking as left state the quantities interpolated from the sampled wind, and as right state the innermost active cell in

**Table 1.** Models evolved and summary of results. The first six models follow the evolution of the system in 2D, including all components (C2d, C2d-res, C2d-src, C2d-h), material interior to 800 km (C2d-df) or just disk material (C2d-d). The second four models explore the properties of fallback accretion in 2D (F2d, F2d-h) and 3D (F3d, F3d-h) neglecting the disk wind. The final five models investigate the effect of injecting the disk wind measured in 2D simulations into a domain containing the dynamical ejecta in 2D (I2d) and 3D (I3d, I3d-nR, I3d-df, I3d-h). The first eight columns from the left show model name, dimensionality, position of the inner and outer radial boundaries, use of viscous and neutrino source terms, injection of disk wind from the inner radial boundary, inclusion of radioactive heating, and type of inner radial boundary condition (out: outflow, rmn: riemann solver, inf: inflow), respectively. The following two columns show the total and unbound mass ejected in wind material (*disk* and *fallback* components) at  $r = 10^9$  cm within 10s, respectively, while the final two columns show the mass-flux-weighted, time-averaged radial velocity and electron fraction of the unbound wind component at  $r = 10^9$  cm, respectively. The black hole has a mass  $M_{\text{bh}} = 11.1M_{\odot}$  and spin parameter  $a = 0.8$  in all cases. See §2.4 for other parameters.

Model	Dim.	$r_{\text{min}}$	$r_{\text{max}}$ (km)	Source Terms	Wind Inj.	Rad. Heat	Bnd. Cnd.	$M_{\text{w,t}}$ ( $10^{-2}M_{\odot}$ )	$M_{\text{w,u}}$ ( $10^{-2}M_{\odot}$ )	$\bar{v}_{\text{w,u}}$ ( $10^{-2}c$ )	$\bar{Y}_{\text{e,u}}$
C2d	2D	37	3.7E+4	Y	...	N	out	3.9	2.1	3.9	0.26
C2d-res					...			3.6	1.7	3.8	0.26
C2d-df					...			3.5	1.5	3.8	0.29
C2d-d					...			3.3	1.6	4.2	0.29
C2d-src <sup>a</sup>					...			4.4	1.4	5.5	0.27
C2d-h					...	Y		4.1	2.4	4.3	0.27
F2d	2D	800	8E+6	N	N	N	out	...	...	...	...
F3d	3D							...	...	...	...
F2d-h	2D					Y		...	...	...	...
F3d-h	3D							...	...	...	...
I3d	3D	800	8E+6	N	Y	N	rmn	1.8	1.4	5.4	0.28
I3d-nR							inf	2.0	1.5	5.1	0.27
I3d-df							rmn	1.0	0.8	5.7	0.28
I3d-h						Y		2.5	1.9	4.9	0.27
I2d	2D							1.5	1.2	7.0	0.28

<sup>a</sup> This model suppresses neutrino and viscous source terms outside  $r = 800$  km.

radius. This is done to account for the possibility that fallback may carry a larger momentum flux than the wind along certain directions. For operational simplicity, we employ the HLLC solver of Toro et al. (1994), which does not require any iterations. As a check, we run a model that simply copies the interpolated values from the 2D simulations into the ghost cells of the 3D domain, without a Riemann solution.

In all cases, if the resulting radial velocity at the ghost cells is negative, a standard outflow boundary condition is adopted: the ghost cells are filled with data from the innermost active cell.

Outside  $r = r_{\text{cut}}$ , the energy source terms that are important for the evolution of the inner disk operate on timescales longer than the expansion time, and are therefore neglected in 3D simulations. To show this, we explicitly evaluate these timescales. The expansion time is

$$t_{\text{exp}} = \frac{r}{v_r} \simeq 0.1 r_8 \left( \frac{0.03c}{v_r} \right) \text{ s}, \quad (2)$$

where  $r_8 = r/10^8$  cm and  $v_r \simeq 0.03c$  for the disk wind (e.g., Fernández et al. 2015). This is comparable to the free-fall time at this radius (for the dynamical ejecta,  $v_r \gtrsim 0.1c$ , which is essentially the Keplerian velocity for a  $10M_{\odot}$  central mass). The viscous time is

$$\begin{aligned} t_{\text{visc}} &\simeq \frac{r^2}{\nu} = \frac{1}{\alpha} \frac{r}{v_K} \left( \frac{H}{R} \right)^{-2} \\ &\simeq 1 \left( \frac{0.03}{\alpha} \right) \left( \frac{H}{R} \right)^{-2} M_{10}^{-1/2} r_8^{3/2} \text{ s}, \end{aligned} \quad (3)$$

where  $\alpha$  is the viscosity parameter of Shakura & Sunyaev

(1973),  $(H/R)$  is the ratio of the disk scaleheight to the local cylindrical radius,  $v_K$  is the Keplerian velocity, and  $M_{10} = M_{\text{bh}}/10M_{\odot}$ . The cooling time is

$$\begin{aligned} t_{\text{cool}} &= \frac{e_{\text{int}}}{Q_{\nu}^-} \simeq \frac{(H/R)^2 v_K^2}{Q_{\nu}^-} \\ &\simeq 400 \left( \frac{H}{R} \right)^2 M_{10} r_8^{-1} \left( \frac{kT}{0.5 \text{ MeV}} \right)^{-6} \text{ s}, \end{aligned} \quad (4)$$

where we have used an approximation to the charged-current weak interaction emissivity from Janka (2001),  $Q_{\nu}^- \simeq 145 (T/2 \text{ MeV})^6 \text{ MeV s}^{-1}$  per baryon, where  $T$  is the local gas temperature. Similarly, the neutrino heating time is

$$\begin{aligned} t_{\text{heat}} &\simeq \frac{(H/R)^2 v_K^2}{Q_{\nu}^+} \\ &\simeq 1 \left( \frac{H}{R} \right)^2 M_{10} r_8 T_{\nu,4}^{-2} L_{\nu,53}^{-1} \text{ s}, \end{aligned} \quad (5)$$

where the approximation for charged-current neutrino absorption by nucleons in Janka (2001) has been used,  $Q_{\nu}^+ \simeq 16 L_{\nu,53} T_{\nu,4} r_7^{-2} \text{ MeV s}^{-1}$  per baryon. Here  $T_{\nu,4}$  is the neutrinosphere temperature in units of 4MeV, and  $L_{\nu,53}$  is the neutrino luminosity in units of  $10^{53} \text{ erg s}^{-1}$ . Finally, the radioactive heating timescale is

$$t_{\text{rad}} \simeq \frac{e_{\text{int}}}{\dot{\epsilon}_0} \simeq 7 \left( \frac{H}{R} \right)^2 M_{10} r_8^{-1} \text{ s}, \quad (6)$$

where  $\dot{\epsilon}_0 = 2 \times 10^{18} \text{ erg/(g s)}$  is the amplitude of the radioactive heating fit of Korobkin et al. (2012).

The hierarchy of timescales at  $r \sim r_{\text{cut}}$  is therefore

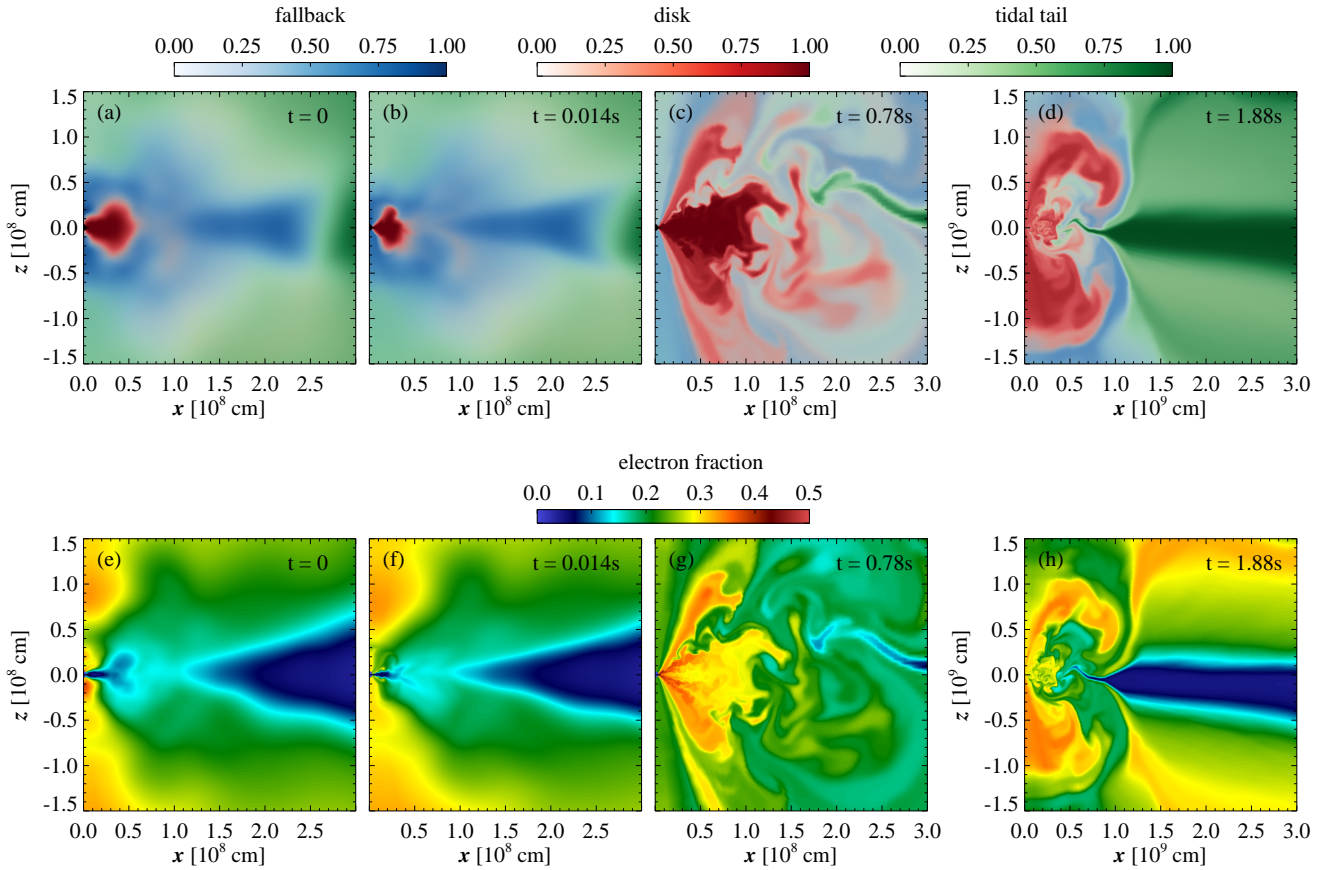


**Figure 2.** Snapshots in the evolution of the high-resolution 2D model C2d-res, which evolves the entire merger remnant (disk + dynamical ejecta) including the effects of shear viscosity and neutrinos. The upper four panels (a-d) show the mass fractions of passive scalars that trace the different components of the system as defined in §2.2: disk (red), fallback (blue), and tidal tail (green). The lower four panels (e-h) show electron fraction. Note the change in  $x$ - and  $z$  scale in panels (d) and (h).

$$t_{\text{exp}} \ll t_{\text{rad}} \sim t_{\text{heat}} \sim t_{\text{visc}} \ll t_{\text{cool}}. \quad (7)$$

Both  $t_{\text{heat}}$  and  $t_{\text{visc}}$  increase as the material expands, whereas  $t_{\text{rad}}$  decreases with increasing radius, at least during the first second of evolution where the heating rate remains nearly constant. This motivates us to include radioactive heating while neglecting neutrino and viscous source terms in 3D simulations covering the region  $r > r_{\text{cut}}$ . While this approximation is strictly valid only for times  $t \lesssim t_{\text{visc}}(r_{\text{cut}}) \sim 1$  s, we adopt it for all times as a first approximation to explore the behavior of the system.

## 2.4 Models evolved

Table 1 summarizes our simulations. We run three sets: one that evolves the complete system in 2D with all the physics (C-series, for “complete”), one that investigates fallback accretion without wind (F-series, for “fallback”), and one that evolves the dynamical ejecta with wind injection from the inner radial boundary (I-series, for “injection”).

The fiducial 2D model (C2d) includes all the axisymmetrized components of the system. This model is repeated at twice the resolution in radius and angle to test for convergence (C2d-res). The next two models test the properties of the disk and wind when excluding all material outside

$r = r_{\text{cut}}$  in the initial condition  $r_{\text{cut}}$  (C2d-df), or including only material tagged initially as *disk* (C2d-d; §2.2). The final two models explore how the system changes when including radioactive heating (C2d-h) and suppressing all source terms outside of  $r = r_{\text{cut}}$  (C2d-src).

Four additional models explore the properties of fallback accretion without wind injection. Two models follow the evolution of all material outside  $r = r_{\text{cut}}$  without source terms other than gravity, one in 2D and one in 3D (F2d and F3d, respectively). Two additional models repeat this calculation, adding radioactive heating (F2d-h and F3d-h).

The last five models explore the interaction of the tidal tail with wind material injected at  $r = r_{\text{cut}}$ . The fiducial 3D model (I3d) uses the wind from model C2d and employs a Riemann boundary condition for injection. A second model (I3d-nR) employs a simpler boundary condition, in which the interpolated wind variables are copied to the ghost cells. A third model (I3d-df) uses the wind sampled from model C2d-df (no tidal tail) and solves a Riemann problem at the boundary. The fourth model (I3d-h) repeats the fiducial model but now adding radioactive heating. Finally, model I2d is the same as I3d but in 2D, for comparison.

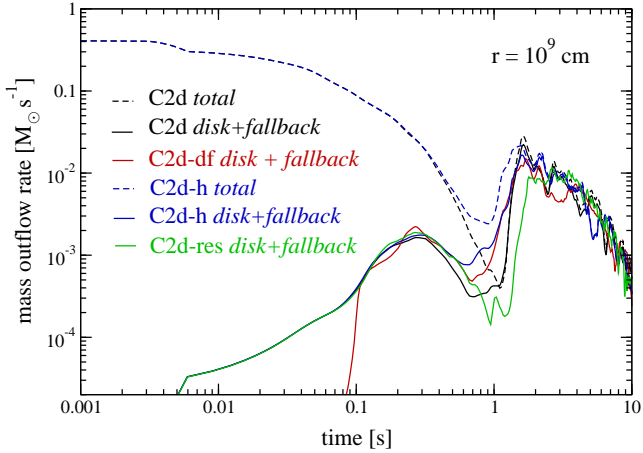


**Figure 3.** Mass outflow rate at  $r = 10^9$  cm as a function of time for different 2D models. The total outflow rate, including the tidal tail, is shown by dashed lines. The ‘wind’ (solid lines) includes material that is tagged as *disk* and *fallback* in the initial condition, as defined in §2.2. The qualitative evolution relative to the baseline model (black) is independent of whether radioactive heating is included (blue), whether the tidal tail is excluded (red), or if the resolution is doubled in radius and polar angle (green).

### 3 RESULTS

#### 3.1 Disk evolution in axisymmetry

Disks formed in mergers involving neutron stars undergo characteristic evolutionary phases determined by the degree of neutrino cooling (e.g. Popham et al. 1999; Narayan et al. 2001; Chen & Beloborodov 2007; Fernández & Metzger 2013a). Neutrino processes are initially important given the high density and temperature of the torus ( $\sim 10^{11}$  g cm $^{-3}$  and  $\sim 5$  MeV, respectively). Despite the high torus mass ( $0.2M_{\odot}$ ), the disk is not too optically thick initially because this mass is spread over a relatively large radial extent (the density maximum is located at  $\sim 80$  km). Given that the initial condition is not in equilibrium and that the microphysics is not the same as that used in the original merger simulation, the system displays a transient phase during the initial  $\sim 0.02$ s (several orbits at the density maximum), adjusting to a new equilibrium state thereafter. The duration of this transient is much shorter than the timescale over which the phenomena we are interested in occur.

Throughout the disk evolution, the contribution of neutrino absorption to the overall heating rate at radii  $r > 100$  km is at most a few per cent of the viscous energy deposition minus neutrino cooling (see also Fernández et al. 2015). We do not see a neutrino-driven wind in our 2D models. Once the disk has spread sufficiently for its temperature and density to drop below values where neutrino cooling becomes inefficient (e.g., Metzger et al. 2009), a viscously-driven outflow is launched. This occurs around  $t \sim 1$  s.

Figure 2 shows how the different components of the system, as traced by passive scalars (§2.2), interact during these evolutionary phases. After a few orbits at the density maximum ( $t = 0.014$ s), during the initial transient phase, the disk reaches a minimum size, presumably due to accretion and compression by fallback material. Once the disk expands due to angular momentum transport and becomes convective, a wind is launched, mixing the original *disk* material

with *fallback* and *tidal tail* matter ( $t = 0.78$  s). At late times, the wind expands primarily towards mid-latitude directions, away from the midplane occupied by the tidal tail ( $t = 1.88$  s). Figure 2 also shows the electron fraction of the different components, contrasting the neutron-rich tidal tail with the higher- $Y_e$  disk wind.

The mass outflow rate as a function of time at a radius of  $10^9$  cm is shown in Figure 3 for models C2d (all components), C2d-df (no tidal tail), C2d-h (radioactive heating), and C2d-res (all components at double resolution in radius and polar angle). The contribution from the *disk* and *fallback* scalars is shown as well as the total mass outflow including tidal tail material. At early times, mass ejection is dominated by the tidal tail, transitioning around  $t \sim 1$  s to dominance by the disk wind. At late times, the instantaneous outflow rate at large radii is not very sensitive to whether the tidal tail is present or not, and whether radioactive heating is included.

Table 1 shows integrated properties of the 2D models over 10 s of evolution. The total mass ejected is of the order of 20 percent of the initial disk mass ( $\sim 0.04M_{\odot}$ ), in agreement with previous results for a BH with spin  $a = 0.8$  (Just et al. 2014; Fernández et al. 2015). The fraction of this outflow that has positive specific energy (with the internal energy normalized so that it vanishes at  $T = 0$ ) lies between 50 and 60 percent. The mean velocity of this unbound wind is  $\sim 0.04c$ . Radioactive heating leads to a  $\sim 15$  percent enhancement in the unbound mass ejection, whereas excluding the tidal tail leads to  $\sim 10$  percent less mass ejected due to the absence of leftover material swept up by the wind. The overall uncertainty due to resolution is  $\sim 10$  percent.

Quantities relevant for heavy-element nucleosynthesis are shown in Table 2. The mass-flux-weighted averages are calculated according to Fernández & Metzger (2013a):

$$\bar{A} = \frac{\int dt d\Omega F_M(r_{\text{out}}, \hat{\Omega}) A(r_{\text{out}}, \hat{\Omega})}{\int dt d\Omega F_M(r_{\text{out}}, \hat{\Omega})}, \quad (8)$$

where  $A$  is a generic quantity,  $F_M = \rho v_r$  is the mass flux,  $\hat{\Omega}$  is the angular direction, and  $r_{\text{out}} \simeq 10^8$  cm is a radius chosen so that  $\bar{T} \simeq 5 \times 10^9$  K when computing the mean  $Y_e$ , entropy, and expansion time. In this case the angular range of the integral is restricted to within  $60^\circ$  of the midplane, because little material populates the polar regions at these radii. In order to compare with 3D models, the average wind velocity and electron fraction shown in Table 1 are computed at  $r = 10^9$  cm, including only material with positive specific energy, and including all angular directions.

The mean electron fraction of the wind is  $\sim 0.26 - 0.29$ , slightly higher than that obtained with a smaller BH mass and more compact disks, starting from an equilibrium initial condition, and using the same neutrino implementation (e.g. Fernández et al. 2015). The mean entropies are  $\sim 30k_B$  per baryon and the expansion time lies in the range 50 – 100 ms. Given these parameters, the critical electron fraction above which no lanthanides are produced is  $\sim 0.25$  (Kasen et al. 2014). The disk wind will therefore lead primarily to lanthanide-free material and a kilonova component peaking in the optical band.

The accretion history at the ISCO is shown in Figure 4. The initial transient phase is evident, with even a short period during which no accretion takes place. From the end of this transient phase at  $t \simeq 0.02$ s until approximately

**Table 2.** Mean properties of the disk wind in 2D models. Columns are model name, electron fraction, entropy, and expansion time. The mass-flux-weighted, time-averaged quantities are computed using equation (8), at a radius where  $\bar{T} \simeq 5 \times 10^9$  K ( $\sim 1000 - 1500$  km). Only material tagged as *disk* and *fallback* is included.

Model	$\bar{Y}_e$	$\bar{s}$ ( $k_B/b$ )	$\bar{t}_{\text{exp}}$ (ms)
C2d	0.29	32	66
C2d-df	0.27	29	111
C2d-d	0.28	29	96
C2d-h	0.28	32	83
C2d-res	0.28	33	48
C2d-src	0.27	29	28

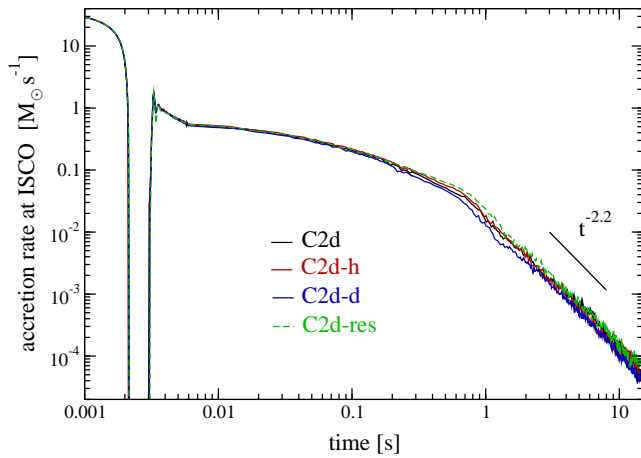


**Figure 4.** Net mass accretion rate at the ISCO for 2D models (see Table 1 for parameters). The late-time accretion rate is somewhat steeper than that due to ballistic fallback, and is set by the viscously spreading disk. The temporal slope does not significantly depend on whether the dynamical ejecta and fallback are excluded, whether radioactive heating is added, or on the resolution of the simulations. At early times ( $t \lesssim 0.01$  s) the disk is undergoing transient readjustment.

$t = 1$  s, the accretion rate evolves smoothly. After the wind is launched, however, the time-dependence of the accretion rate steepens, with the asymptotic power-law in the range  $t^{-2.15} - t^{-2.3}$ . Such a drop in the accretion rate at late times was first seen by Lee et al. (2009). In the context of fallback accretion, we note that this time-dependence is insensitive to whether material labeled as *fallback* and *tidal tail* is included, as shown in Figure 4 (model C2d-d includes only material labeled as *disk*).

Indeed, one can show using simple scaling arguments that during the late radiatively-inefficient phase of evolution, the mass accretion rate scales like  $t^{-4/3}$  (Metzger, Piro & Quataert 2008). This scaling becomes even steeper ( $t^{-8/3}$ ) when outflows are included in the solution. Our models have an intermediate behavior between these two limits.

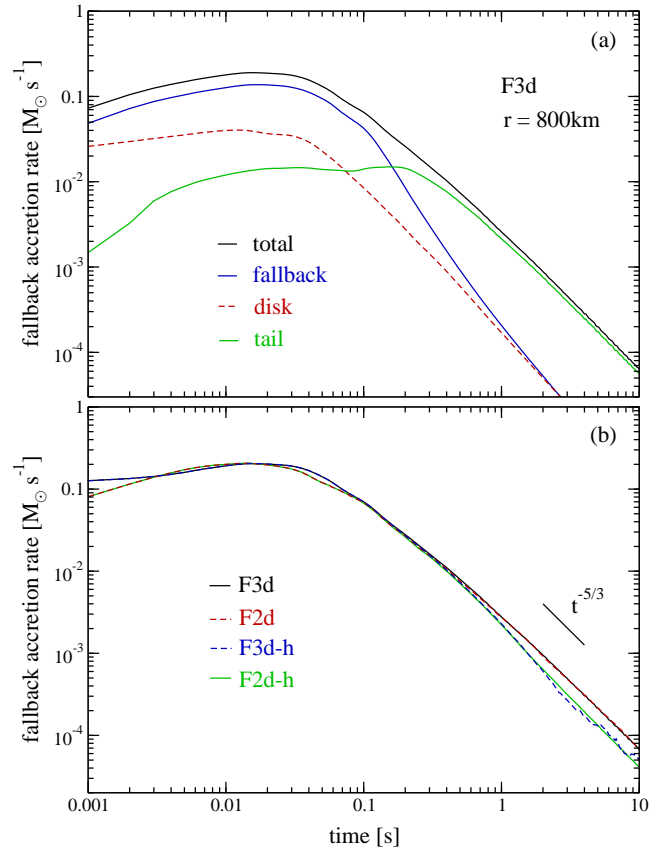


**Figure 5.** Mass accretion (fallback) rate as a function of time at  $r = r_{\text{cut}} = 800$  km for models without wind injection. Panel (a) shows the accretion rate for model F3d, which ignores radioactive heating. Also shown are the contributions from the different components of the system (§2.2) as traced by passive scalars. Panel (b) compares 2D and 3D models with and without radioactive heating. While radioactive heating causes a temporary steepening of the accretion rate with time, its overall effect is small. Models in 2D and 3D are very close to each other at late times.

### 3.2 Fallback accretion without disk wind: effect of radioactive heating

If the gravitationally bound part of the dynamical ejecta moves in Keplerian orbits, the expected fallback accretion scales with time like (e.g., Rees 1988)

$$\dot{M}_f \propto \frac{dM}{dE_{\text{orb}}} t^{-5/3}, \quad (9)$$

where  $dM/dE_{\text{orb}}$  is the distribution of ejected mass with orbital energy. For orbits with durations longer than the  $r$ -process ( $\sim 1$  s), the energy deposited by radioactive heating can exceed the orbital binding energy (Metzger et al. 2010a). Given the parameters of our simulation, this would occur for simulation times

$$t \simeq 4 \left( \frac{M}{11.1 M_{\odot}} \right) \left( \frac{2 \text{ MeV}}{E_r} \right)^{3/2} \text{ s}, \quad (10)$$

where  $E_r$  is the energy deposited by the  $r$ -process. For a range  $E_r = 1 - 3$  MeV, the affected times are 2 – 11 s.

Figure 5a shows the mass accretion rate at the inner radial boundary of the 3D computational domain ( $r = r_{\text{cut}} = 800$  km) for model F3d, which does not include the effect of



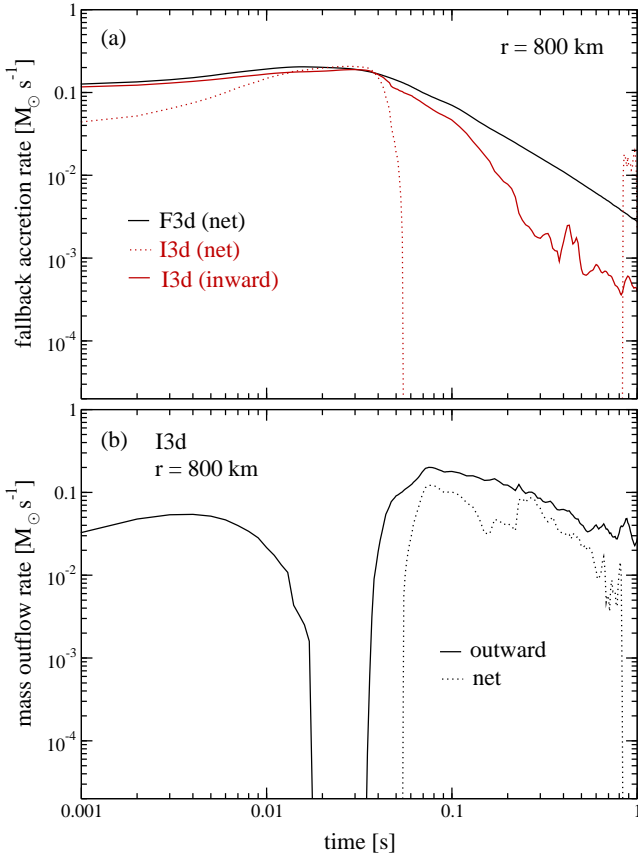


**Figure 6.** *Panel (a)*: accretion rate at  $r = r_{\text{cut}} = 800$  km in models that evolve the dynamical ejecta in 3D with wind injection (I3d) and without wind (F3d). The curve labeled ‘inward’ includes only material initially present in the domain and with negative radial velocity at the inner boundary, for comparison with the model without wind. The net accretion rate for model I3d includes all material. *Panel (b)*: Mass outflow rate in the fiducial model I3d. Shown are the total amount of material with positive velocity injected into the domain (‘outward’) and the net outflow rate including all material. The first outflow episode ( $t < 0.02$  s) corresponds to dynamical ejecta material moving outward, with the second caused by the disk wind (c.f. Figure 3).

the disk wind or radioactive heating, instead simply letting all material evolve under the effects of gravity. The accreted material at  $r = 800$  km is initially composed primarily of fluid tagged as *fallback*. Around  $t = 2$  s, the composition becomes dominated by *tidal tail* material. As pointed out in §2.2, approximately  $0.01M_{\odot}$  of tidal tail material is gravitationally bound due to spatial overlap with other components. This material is almost completely accreted during the simulated time.

The accretion rate at  $r = r_{\text{cut}}$  in all models that do not include the disk wind is shown Figure 5b. Models F2d and F3d (no radioactive heating) differ slightly in their initial evolution until  $\sim 1$  s, after which they display a nearly identical accretion history. The fact that the time dependence of this accretion is very nearly  $t^{-5/3}$  indicates that the mass distribution is close to uniform in orbital energy, and that the contribution from the fluid pressure to the dynamics is minor.

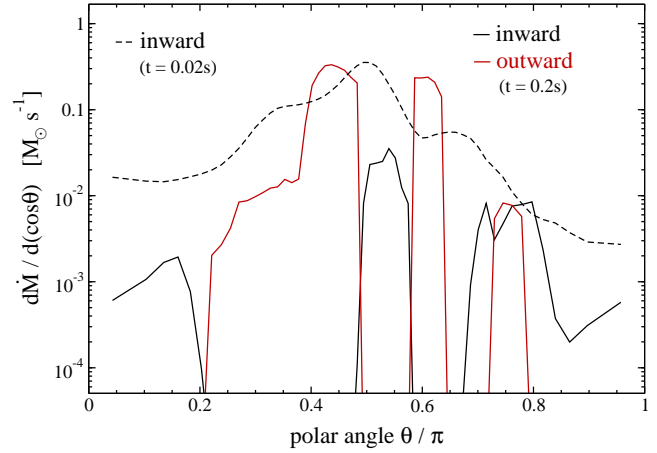


**Figure 7.** Distribution of the mass flow rate at  $r = r_{\text{cut}}$  as a function of polar angle (eq. 11) for the fiducial 3D model with wind injection (I3d) at two times. The inward accretion rate includes only material initially present in the domain and which has negative radial velocity at the inner radial boundary. The outflow rate includes only material injected into the domain. Compare with Fig. 6.

Including radioactive heating modifies the evolution of the accretion rate on the expected timescales (eq. [10]) by steepening the time-dependence over the interval  $0.3 - 3$  s. This is shown in Figure 5b, where models F2d-h and F3d-h are shown alongside models that do not include heating. While a gap in the fallback rate, as envisioned by Metzger et al. (2010a), does not appear, the accretion rate is suppressed over a finite interval relative to the case without heating, returning later to the approximate  $t^{-5/3}$  scaling. The absence of a gap can be explained by the constancy of  $dM/dE_{\text{orb}}$  (equation 9) as inferred from the models without radioactive heating. Addition of energy by the  $r$ -process simply shifts mass in this distribution towards higher energies, filling the gap near  $E_{\text{orb}} = 0$  with material that initially had lower energy.

The total accreted material for all models in this sequence lies in the range  $0.026 - 0.029M_{\odot}$ . If the accretion rate were to continue indefinitely with the same magnitude and scaling as it has at  $t = 10$  s, only an additional  $\sim 10^{-4}M_{\odot}$  would be added.

### 3.3 Effect of disk wind on fallback accretion

The disk wind causes important changes in the properties of fallback accretion. This was already seen in the 2D results of §3.1, where the disk completely dominates over fallback material in setting the late-time accretion rate (Fig. 4). Here we examine this interplay using more realistic 3D simulations, in which the wind measured in 2D models is injected from the inner radial boundary at  $r = r_{\text{cut}} = 800$  km. Figure 6a compares the evolution of the mass accretion rate in our 3D simulations with and without wind. We isolate material that is initially outside  $r = r_{\text{cut}}$  by assigning a passive scalar  $X_{\text{inj}} = 1$  to all material that is subsequently injected into the domain, independent of which component of the system (§2.2) it is made of. We then compute the total mass flux with negative radial velocity at the inner boundary, multiply by  $(1 - X_{\text{inj}})$ , and integrate in solid angle. Figure 6 shows

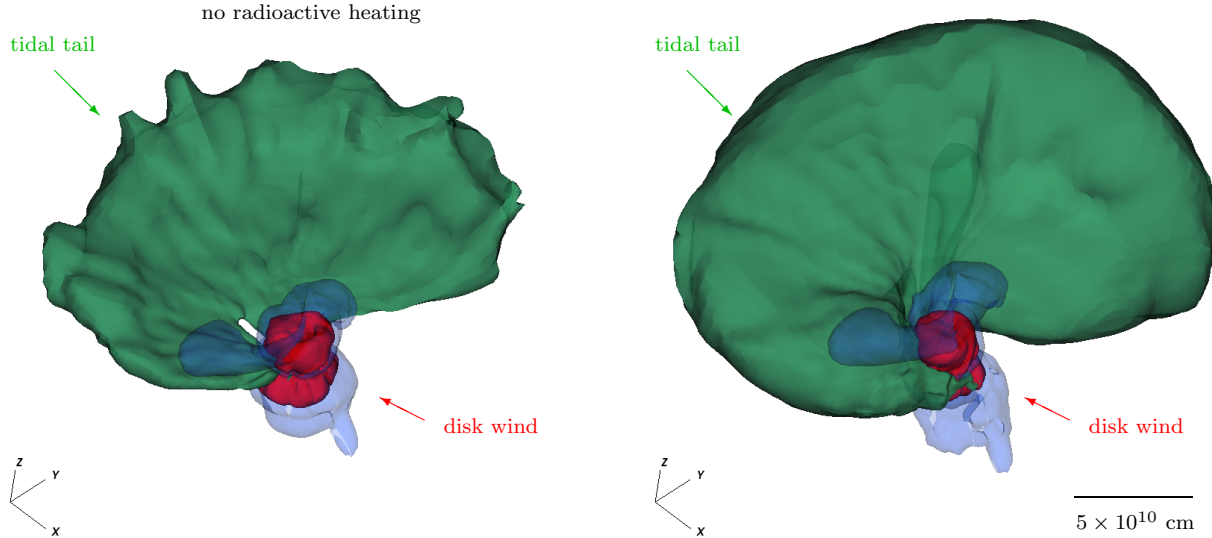


**Figure 8.** Isosurfaces of passive scalars tracing material initially tagged as *tidal tail* (90% mass fraction, green) and *wind* (*disk+fallback*) (5% and 95% mass fraction, blue and red, respectively) at time  $t = 10$  s. Shown are the fiducial 3D model of dynamical ejecta evolution with disk wind injection from the inner boundary (I3d, left) and a version that adds radioactive heating by the  $r$ -process (I3d-h, right). Most of the material shown is already in homologous expansion, hence its geometry will not change at later times.

that fallback accretion is suppressed after  $t \sim 100$  ms when the wind is injected.

Small quantitative modifications in the evolution of the accretion rate around and after the onset of the wind are obtained when including radioactive heating, when using a different treatment for the wind injection, and when using the wind from model C2d-df, which does not include the feedback from the tidal tail in 2D (c.f. Table 1).

The net accretion rate (all material) at  $r = r_{\text{cut}}$  for the fiducial model is also shown in Figure 6a. Initially, this net accretion rate is lower than the case with no wind injection. This decrease is caused by dynamical ejecta material moving outward, as shown in Figure 6b. Once this initial outflow subsides, the net accretion rate reaches its full magnitude around  $t \sim 30$  ms. Shortly thereafter, the net accretion rate becomes net outflow once the wind turns on.

Figure 7 illustrates the simultaneous flow of wind material and fallback accretion at  $r = r_{\text{cut}}$ . Shown are snapshots of the mass inflow and outflow rate as a function of polar angle,

$$\frac{d\dot{M}}{d(\cos\theta)} = \int d\phi r_{\text{cut}}^2 f_{\text{inj}} \rho v_r, \quad (11)$$

with  $f_{\text{inj}} = X_{\text{inj}}$  for outward moving material ( $v_r > 0$ ) and  $f_{\text{inj}} = (1 - X_{\text{inj}})$  for  $v_r < 0$ . At  $t = 0.2$  s, accretion proceeds primarily along the equator, with the wind flowing towards mid-latitudes. This segregation is not persistent, however, with a different distribution in angle at later times. Note also that accretion and wind can co-exist at different azimuthal angles (e.g.  $\theta \simeq 3\pi/4$ ).

At about  $t \sim 1$  s, our diagnostic for the inflow at  $r = r_{\text{cut}}$  shows that net accretion resumes, with strong stochastic fluctuations (Fig. 6a). This is, however, related to the spreading of the accretion disk outside  $r = 800$  km. In other words, the outer edge of the radiatively-inefficient,

convective accretion disk enters the 3D computational domain, with the wind-launching radius moving continuously outward<sup>1</sup>.

### 3.4 Properties of the disk wind and dynamical ejecta at large radii

By the end of our simulations, at  $t = 10$  s, the system is approaching homology: the material outside  $r \simeq 2 \times 10^{10}$  cm has radial velocity roughly proportional to radius ( $\sim r^{0.95}$ ). This material amounts to 60 percent of the mass in the computational domain.

The geometry of this homologous ejecta is shown in Figure 8. The tidal tail wraps around the rotation axis, occupying primarily the equatorial plane. The wind is located at the center of the domain, expanding towards high- to intermediate latitudes. Because the wind is expanding more slowly than the dynamical ejecta by a factor of several, in the homologous limit its spatial extent must be smaller by the same factor.

Including radioactive heating smoothes inhomogeneities in the tidal tail, increasing its vertical extent due to the added thermal energy, as shown in Figure 8. This result is consistent with the findings of Rosswog et al. (2014). In terms of the expected electromagnetic counterpart, this implies that neutron-rich (and hence high-opacity) material in the tidal tail obscures the disk wind component for a larger set of viewing angles along the equator (e.g., Kasen et al. 2014), relative to the case without radioactive heating. Given this particular set of initial conditions, however, the tidal tail does not cover all azimuthal angles, hence

<sup>1</sup> While the position of the outer edge of the disk is not uniquely defined, we estimate it by computing an isodensity surface at  $10^{-4}$  times the instantaneous density maximum.

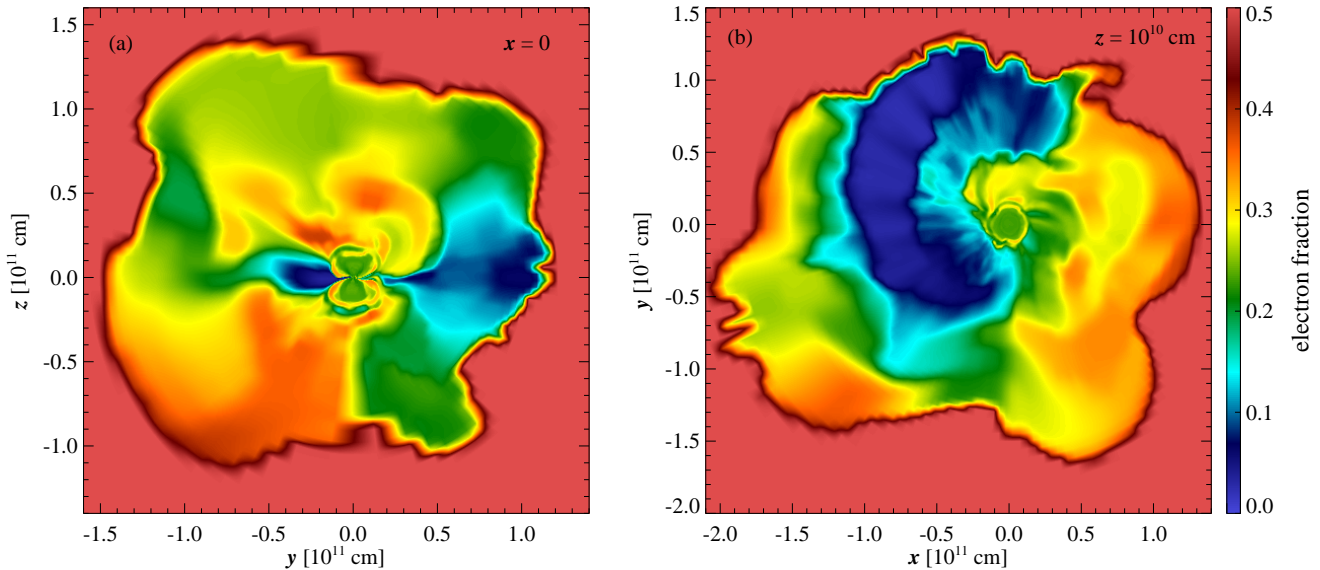


**Figure 9.** Electron fraction in the fiducial 3D model I3d at time  $t = 10$  s. Shown are two-dimensional slices normal to the  $x$ -axis (a) and normal to the  $z$ -axis (b). Compare with Figure 8.

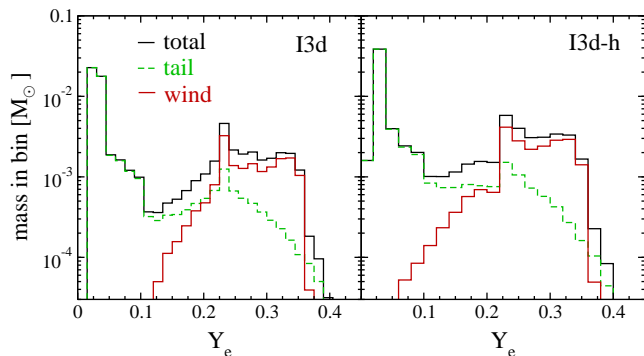


**Figure 10.** Mass histograms as a function of electron fraction for models I3d and I3d-h (c.f. Figure 9). The histograms are computed by summing all the material crossing the radius  $r = 3 \times 10^9$  cm over the entire simulation time ( $t = 10$  s).

the expected optical emission from the disk wind can readily escape along those unobstructed viewing directions.

The material in the tidal tail is significantly more neutron rich than that in the disk wind, as is well-known. Figure 9 shows slices of the electron fraction distribution normal to the  $x$  and  $z$  axes, illustrating the spatial distribution of material that will give rise to Lanthanide-rich ( $Y_e \lesssim 0.25$ ) and Lanthanide-poor ejecta ( $Y_e \gtrsim 0.25$ ; see, e.g., Kasen et al. 2014). Figure 10 shows a mass histogram as a function of electron fraction for models I3d and I3d-h, including all material crossing a surface at  $r = 3 \times 10^9$  cm. The histograms are bimodal, with clear contributions from the tidal tail at  $Y_e \lesssim 0.05$ , and disk wind at  $Y_e \sim 0.25$ . At small amount of tidal tail material is mixed with the wind, and has higher electron fraction.

Our method of injecting the wind from the inner radial boundary works well as long as the disk does not enter the computational domain. Once the disk enters, around  $t \sim 1$  s, there is a discrepancy between the stresses at this bound-

ary and those that would be obtained in a self-consistent simulation. In particular, the use of an outflow boundary condition whenever the radial velocity at the boundary is negative leads on average to lower pressure support on the section of the disk that has entered the domain.

The consequence of this discrepancy in stresses is a decrease in the amount of mass ejected to large radius in models with wind injection relative to a self-consistent simulation. Table 1 shows that this discrepancy is a factor of  $\sim 2$ , and is independent of whether 2D or 3D is employed (model I2d vs. C2d) or whether neutrino and viscous source terms are included in the self-consistent model (models C2d vs. C2d-src).

We can nevertheless still compare the bulk properties of the wind at large radius between 3D models, using the 2D model with wind injection (I2d) as a baseline. Table 1 shows that the specific wind injection method (solving a Riemann problem or simply filling the ghost cells with the sampled wind) is largely unimportant in determining the wind properties at a radius  $r = 10^9$  cm. Including radioactive heating does indeed lead to more mass ejection, with an enhancement similar to that observed in the 2D models. Similarly, injecting the wind sampled from model C2d-d (no tidal tail) leads to correspondingly small mass ejection.

The velocity and electron fraction of the wind undergo small changes relative to 2D. While both increase relative to the 2D models, the change is not likely to lead to qualitative differences in their nucleosynthetic properties and in their effect on the observed kilonova. In the case of the electron fraction, this implies that there is no significant mixing between wind material and the bulk of the dynamical ejecta, which would otherwise have lowered  $Y_e$  from its pure wind value. While Figure 8 indicates that some mixing does indeed occur in the immediate vicinity of the wind, the amount of mass affected is a small fraction of the total, and goes in the direction of making tidal tail material more proton rich

(Figure 10). This low degree of mixing is a consequence of the factor 2–4 faster radial velocity of the dynamical ejecta.

#### 4 SUMMARY AND DISCUSSION

We have investigated the interaction between the disk wind and dynamical ejecta generated in a NS - BH merger. Starting from the output of a Newtonian merger simulation, we have disentangled the ejecta components using its phase space distribution (§2.2). The disk is located at small radii and is nearly axisymmetric, hence the resulting disk wind can be estimated from axisymmetric simulations to first approximation. Given that viscous and neutrino source terms are sub-dominant in the outer regions of the system, where the non-axisymmetric dynamical ejecta resides, one can evolve this component in 3D without the high computational cost of viscous or neutrino processes. We therefore inject the axisymmetric disk wind from the inner boundary of the 3D computational domain.

By following this two-step approach, we obtain the following results:

1. – Fallback accretion can be suppressed once the disk wind is launched (Fig. 6). In our models, this happens  $\sim 100$  ms into the simulation.
2. – The properties of the disk wind are not significantly affected by the dynamical ejecta. This is largely due to the difference in expansion velocities. Most of the gravitationally bound part of the dynamical ejecta (‘fallback’, §2.2) is swept up by the wind, forming its leading edge (Fig. 2d). While some small amount of mixing occurs between material coming from the disk and that in the tidal tail, it goes primarily in the direction of making tidal tail material more proton rich (Fig. 10).
3. – The time dependence of the mass accretion rate at the ISCO steepens after the wind is launched. For our choice of parameters, it follows a slope  $\sim t^{-2.2}$  (Fig. 4). This is nearly independent of whether the *tidal tail* and *fallback* components are included in the simulation. This power-law decline is set by the physics of the viscously spreading disk with outflows (Metzger et al. 2008), not fallback.
4. – We do not find a gap in the fallback accretion rate induced by radioactive heating when the wind is ignored (Fig. 5). Instead, we find a steepening in the time-dependence of this accretion rate over a finite interval, resuming the quasi-ballistic  $t^{-5/3}$  time-dependence at late times. Inclusion of radioactive heating in disk wind simulations yields a small ( $\sim 10\%$ ) enhancement in the ejected mass (Table 1), with no qualitative differences in the ejecta composition (Table 2).
5. – We find that including radioactive heating smoothes out inhomogeneities in the tidal tail (Fig. 8), in agreement with Rosswog et al. (2014). This results in very neutron-rich material (with high optical opacity) obscuring a larger fraction of the available viewing directions towards the wind ejecta, which has a smaller size in the homologous limit due to its smaller velocity. However, the specific model we evolved is

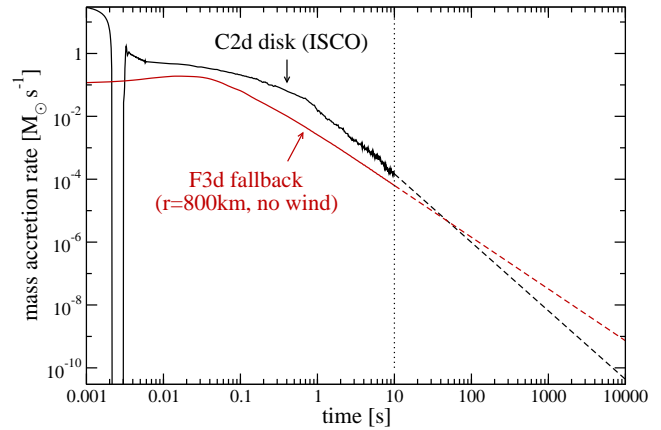


**Figure 11.** Extrapolation of the mass accretion rate from disk accretion at the ISCO (black, model C2d) and fallback with no wind at  $r = 800$  km (red, model F3d) after  $t = 10$  s, illustrating the smaller energy released by the disk at times where extended GRB central engine emission and/or X-ray flares takes place.

such that the tidal tail does not cover all azimuthal angles (Fig. 9), leaving a wide range of unobstructed sight lines.

6. – The properties of the disk outflow are qualitatively similar to those obtained from simulations with spinning BHs that begin from idealized initial conditions with somewhat less massive and more compact disks (e.g., Fernández et al. 2015).

While our quantitative results are specific to the particular initial condition we have adopted, our approach contains several features that can be useful in future studies of the interplay between the different components of the combined merger ejecta. First, we have found a novel way to isolate the dynamical ejecta – bound and unbound gravitationally – from rotationally supported material. Second, we have shown that ignoring neutrino and viscous source terms at large radii ( $r \gtrsim 10^8$  cm) has a minor effect on the evolution of the system. The main drawback of our method is the treatment of the boundary condition when the radial velocity is negative. At times  $t \gtrsim 1$  s, the disk has spread out sufficiently to enter our 3D domain. If the stresses ensuing from this boundary condition are not sufficient to support the part of the disk inside the domain, an excess of mass will flow inwards, significantly affecting the amount of wind launched to large radii. Large-domain axisymmetric simulations are a reasonable way to improve this analysis, given the similarity in the globally integrated properties.

The fact that we have found no significant mixing between the disk wind and dynamical ejecta means that separately estimating the nucleosynthetic contribution from the disk and tidal tail is a reasonable approximation. This is relevant given that the two components are expected to lead to different nucleosynthetic signatures, with implications for the dispersion in the  $r$ -process abundance in the galaxy (Just et al. 2014) and the properties of the kilonova emission (Metzger & Fernández 2014, Kasen et al. 2014).

Even though our results show that fallback accretion is not always a robust source of late-time engine activity in short GRBs, the fact that accretion from the disk contin-

ues for a long time provides a persistent source of accretion power. However, the steeper decline with time in the accretion rate relative to ballistic fallback ( $t^{-2.2}$  vs.  $t^{-5/3}$ ) implies that after  $10^4$  s, the energy output from accretion is  $\sim 30$  times smaller (disk accretion is  $\sim 3$  times larger than wind-free fallback at  $t = 1$  second, cf. Figs. 4 and 5). This is illustrated in Figure 11, which shows the extrapolation of the mass accretion rate at the ISCO for the default 2D model C2d, together with the extrapolation of the fallback accretion rate (without the effect of the disk wind) at  $r = 800$  km from model F3d. The extrapolation of the fallback rate is an upper limit, however, given that material has angular momentum and may circularize at a radius larger than the ISCO. In this case, material will contribute to whatever remains of the disk and accretion will proceed at a rate set by viscous processes, eventually acquiring a  $t^{-2.2}$  time dependence. Even if fallback material has low angular momentum, the presence of the disk will prevent it from falling directly onto the BH, particularly along the midplane.

If accretion indeed dominates late-time engine activity, time-variability can result if instabilities occur in the outer disk (Perna et al. 2006) or near the black hole due to magnetic effects (Proga & Zhang 2006). Even if accretion is smooth, late-time variability can result if the surrounding medium is excavated by Poynting flux if the neutron star is a pulsar before the merger (Holcomb et al. 2014).

The observed suppression of fallback in our models is contingent on the initial condition we have chosen to carry out our study, and hence it is not necessarily a general property of NS-NS or NS-BH mergers. In our simulations, the amount of mass ejection in the wind ( $0.04M_{\odot}$ , or  $\sim 20\%$  of the initial disk mass) is larger than the initial amount of fallback and bound tidal tail material ( $0.03M_{\odot}$ ). Inclusion of general relativity and a slightly different set of binary parameters (including eccentricity; East et al. 2012) can in principle lead to a different hierarchy. For example, Foucart et al. (2014) find disk masses in the range  $0.04 - 0.14M_{\odot}$  and bound dynamical ejecta in the range  $0.03 - 0.05$  when considering mergers of neutron stars with  $7M_{\odot}$  BHs in general relativity. Their lowest disk mass is a factor 5 smaller than ours, and the expected fallback is a factor  $\sim 2$  larger. In this case, does the disk wind escape at intermediate latitudes while fallback proceeds and keeps the mass supply constant? Or does fallback suppress the onset of the wind, entraining material back to the disk?

In the case of NS-NS mergers, the dynamical ejecta is less concentrated in the midplane than in BH-NS mergers of large mass ratio (e.g. Bauswein et al. 2013; Hotokezaka et al. 2013). For similar relative masses between bound dynamical ejecta and disk, the more spherical geometry should make it easier for the disk wind to disrupt fallback.

Our calculations can be improved in many ways. Injection of the wind into an expanding boundary in 3D models would alleviate the problems introduced when the disk enters the domain, and allow a better estimate of the degree of mixing between tidal tail and disk. The wind calculations can be made more realistic by including MHD and GR effects self-consistently. The composition of the wind can be better quantified by using an improved neutrino transport scheme. The contribution of radioactive heating to the dynamics of fallback material can be studied further by ac-

counting for the increase in temperature of fluid elements as they fall towards the BH (the prescription we employed assumes that all fluid elements are in continuous expansion, thus overestimating the energy release). Future studies will address these improvements.

## ACKNOWLEDGMENTS

We thank Brian Metzger, Frank Timmes, and the anonymous referee for constructive comments that improved the paper. RF acknowledges support from the University of California Office of the President, and from NSF grant AST-1206097. EQ was supported by NSF grant AST-1206097, the David and Lucile Packard Foundation, and a Simons Investigator Award from the Simons Foundation. JS is supported by the National Science Foundation Graduate Research Fellowship Program under Grant No. DGE 1106400. DK was supported in part by a Department of Energy Office of Nuclear Physics Early Career Award, and by the Director, Office of Energy Research, Office of High Energy and Nuclear Physics, Divisions of Nuclear Physics, of the U.S. Department of Energy under Contract No. DE-AC02-05CH11231. SR was supported by the Deutsche Forschungsgemeinschaft (DFG) under grant RO-3399, AOBJ-584282 and by the Swedish Research Council (VR) under grant 621-2012-4870. The software used in this work was in part developed by the DOE NNSA-ASC OASCR Flash Center at the University of Chicago. This research used resources of the National Energy Research Scientific Computing Center (NERSC), which is supported by the Office of Science of the U.S. Department of Energy under Contract No. DE-AC02-05CH11231. Computations were performed at *Carver* and *Hopper* (repos m1186, m1896, and m2058).

## REFERENCES

- Abadie J., et al., 2010, *Classical and Quantum Gravity*, 27, 173001
- Artemova I. V., Bjoernsson G., Novikov I. D., 1996, *ApJ*, 461, 565
- Barnes J., Kasen D., 2013, *ApJ*, 775, 18
- Bauswein A., Goriely S., Janka H.-T., 2013, *ApJ*, 773, 78
- Berger E., 2014, *ARA&A*, 52, 43
- Chen W.-X., Beloborodov A. M., 2007, *ApJ*, 657, 383
- Dessart L., Ott C. D., Burrows A., Rosswog S., Livne E., 2009, *ApJ*, 690, 1681
- Dubey A., Antypas K., Ganapathy M. K., Reid L. B., Riley K., Sheeler D., Siegel A., Weide K., 2009, *J. Par. Comp.*, 35, 512
- East W. E., Pretorius F., Stephens B. C., 2012, *Phys. Rev. D*, 85, 124009
- Faber J. A., Baumgarte T. W., Shapiro S. L., Taniguchi K., 2006, *ApJ*, 641, L93
- Farr W. M., Sravan N., Cantrell A., Kreidberg L., Bailyn C. D., Mandel I., Kalogera V., 2011, *ApJ*, 741, 103
- Fernández R., 2012, *ApJ*, 749, 142
- Fernández R., Kasen D., Metzger B. D., Quataert E., 2015, *MNRAS*, 446, 750
- Fernández R., Metzger B. D., 2013a, *MNRAS*, 435, 502
- Fernández R., Metzger B. D., 2013b, *ApJ*, 763, 108
- Foucart F., 2012, *PRD*, 86, 124007
- Foucart F., Deaton M. B., Duez M. D., O'Connor E., Ott C. D., Haas R., Kidder L. E., Pfeiffer H. P., Scheel M. A., Szilagyi B., 2014, *PRD*, 90, 024026

- Freiburghaus C., Rosswog S., Thielemann F., 1999, *ApJ*, 525, L121
- Fryxell B., Olson K., Ricker P., Timmes F. X., Zingale M., Lamb D. Q., MacNeice P., Rosner R., Truran J. W., Tufo H., 2000, *ApJS*, 131, 273
- Gehrels N., et al., 2006, *Nature*, 444, 1044
- Goriely S., Sida J.-L., Lemaître J.-F., Panebianco S., Dubray N., Hilaire S., Bauswein A., Janka H.-T., 2013, *Physical Review Letters*, 111, 242502
- Holcomb C., Ramirez-Ruiz E., De Colle F., Montes G., 2014, *ApJ*, 790, L3
- Hotokezaka K., Kiuchi K., Kyutoku K., Okawa H., Sekiguchi Y.-i., Shibata M., Taniguchi K., 2013, *Phys. Rev. D*, 87, 024001
- Janka H.-T., 2001, *A&A*, 368, 527
- Just O., Bauswein A., Ardevol Pulpillo R., Goriely S., Janka H.-T., 2014, *MNRAS*, in press, arXiv:1406.2687
- Kasen D., Badnell N. R., Barnes J., 2013, *ApJ*, 774, 25
- Kasen D., Fernández R., Metzger B., 2014, *MNRAS*, submitted, arXiv:1411.3726
- Korobkin O., Rosswog S., Arcones A., Winteler C., 2012, *MNRAS*, 426, 1940
- Kyutoku K., Ioka K., Shibata M., 2013, *PRD*, 88, 041503
- Lattimer J. M., Schramm D. N., 1974, *ApJ*, 192, L145
- Lee W. H., Ramirez-Ruiz E., López-Cámara D., 2009, *ApJ*, 699, L93
- Li L., Paczyński B., 1998, *ApJ*, 507, L59
- McLaughlin G. C., Surman R., 2005, *Nuclear Physics A*, 758, 189
- Metzger B. D., Arcones A., Quataert E., Martínez-Pinedo G., 2010a, *MNRAS*, 402, 2771
- Metzger B. D., Fernández R., 2014, *MNRAS*, 441, 3444
- Metzger B. D., Martínez-Pinedo G., Darbha S., Quataert E., Arcones A., Kasen D., Thomas R., Nugent P., Panov I. V., Zinner N. T., 2010b, *MNRAS*, 406, 2650
- Metzger B. D., Piro A. L., Quataert E., 2008, *MNRAS*, 390, 781
- Metzger B. D., Piro A. L., Quataert E., 2009, *MNRAS*, 396, 304
- Narayan R., Piran T., Kumar P., 2001, *ApJ*, 557, 949
- Özel F., Psaltis D., Narayan R., McClintock J. E., 2010, *ApJ*, 725, 1918
- Perego A., Rosswog S., Cabezón R. M., Korobkin O., Käppeli R., Arcones A., Liebendörfer M., 2014, *MNRAS*, 443, 3134
- Perna R., Armitage P. J., Zhang B., 2006, *ApJ*, 636, L29
- Popham R., Woosley S. E., Fryer C., 1999, *ApJ*, 518, 356
- Proga D., Zhang B., 2006, *MNRAS*, 370, L61
- Rees M. J., 1988, *Nature*, 333, 523
- Rosswog S., 2007, *MNRAS*, 376, L48
- Rosswog S., Korobkin O., Arcones A., Thielemann F.-K., Piran T., 2014, *MNRAS*, 439, 744
- Rosswog S., Liebendörfer M., 2003, *MNRAS*, 342, 673
- Rosswog S., Piran T., Nakar E., 2013, *MNRAS*, 430, 2585
- Shakura N. I., Sunyaev R. A., 1973, *A&A*, 24, 337
- Shen H., Toki H., Oyamatsu K., Sumiyoshi K., 1998, *Nuc. Phys. A*, 637, 435
- Surman R., McLaughlin G. C., Hix W. R., 2006, *ApJ*, 643, 1057
- Surman R., McLaughlin G. C., Ruffert M., Janka H.-T., Hix W. R., 2008, *ApJ*, 679, L117
- Tanaka M., Hotokezaka K., 2013, *ApJ*, 775, 113
- Tanaka M., Hotokezaka K., Kyutoku K., Wanajo S., Kiuchi K., Sekiguchi Y., Shibata M., 2014, *ApJ*, 780, 31
- Timmes F. X., Swesty F. D., 2000, *ApJS*, 126, 501
- Toro E. F., Spruce M., Speares W., 1994, *Shock Waves*, 4, 25
- Wanajo S., Janka H.-T., 2012, *ApJ*, 746, 180